DOI: 10.17344/acsi.2020.5857 *Acta Chim. Slov.* **2020,** *67,* 1082–1091

Scientific paper

Visible Light-Driven Photocatalytic Activity of Magnetic Recoverable Ternary $ZnFe_2O_4$/rGO/g-C_3N_4 Nanocomposites

Martin Tsvetkov,[1,*] Elzhana Encheva,[1] Albin Pintar,[2] and Maria Milanova[1]

[1] *Department of Inorganic Chemistry, Faculty of Chemistry and Pharmacy, St. Kl. Ohridski University of Sofia, J. Bourchier 1, 1164 Sofia, Bulgaria*

[2] *Laboratory for Environmental Sciences and Engineering, National Institute of Chemistry, Hajdrihova 19, 1001 Ljubljana, Slovenia*

* *Corresponding author: E-mail: mptsvetkov@gmail.com*

Received: 01-25-2020

Abstract

$ZnFe_2O_4$/rGO/g-C_3N_4 ternary nanocomposite photocatalysts with different $ZnFe_2O_4$/g-C_3N_4 weight ratio (0.5, 0.75, 1) were prepared by a stepwise solvothermal method using ethylene glycol as the solvent. Physicochemical methods such as X-ray diffraction, UV-Vis diffuse reflectance spectroscopy and photoluminescence spectroscopy were applied in order to characterize the composites. The formation of a meso-/macroporous structure with specific surface area between 67 and 77 m^2 g^{-1} was confirmed by N_2 adsorption/desorption. The bandgap of the composites was found to be lower (2.30 eV) than that of g-C_3N_4 (2.7 eV). In contrast to pure g-C_3N_4, the composites showed no fluorescence, i.e. no recombination of e^-/h^+ took place. All samples, including pure g-C_3N_4 and $ZnFe_2O_4$, were tested for adsorption and photocatalytic degradation of aqueous malachite green model solutions (10^{-5} M) under visible light irradiation ($\lambda > 400$ nm). The results show that the prepared nanocomposites have higher absorption and photocatalytic activity than the pristine g-C_3N_4 and $ZnFe_2O_4$ and can be successfully used for water purification from organic azo-dyes.

Keywords: Graphitic carbon nitride; reduced graphene oxide; zinc ferrite; photocatalysis; malachite green decomposition.

1. Introduction

Synthetic organic dyes are severe water pollutants causing environmental problems. They are typically aromatic compounds with structural variations, many of them resistant to degradation.[1] Among them, malachite green is an organic water pollutant known to be harmful for living creatures because of its potential carcinogenicity, mutagenicity and teratogenicity in mammals.[2] Depending on the polluted water composition, different methods have been applied in order to solve water contamination problems, including biological reactions,[3] sedimentation,[4–6] coagulation,[7,8] adsorption,[5] reverse osmosis,[9,10] membrane filtration,[11] ion exchange,[12] etc. Photocatalytic processes have also been applied, and much effort has been spent on the development of different semiconductors as photocatalysts among which TiO_2 and its modifications is well known.[13-18]

The aim of the research presented here is to develop new photocatalysts and to overcome the main limitation of TiO_2, i.e. its wide band gap (3.2 eV) that makes it active under UV light irradiation only (about 5% of sunlight). Recently the graphite analogue, graphitic carbon nitride, g-C_3N_4, raised interest due to its unique electronic structure. It is a non-metallic polymer with n-type semiconducting behavior and unique electrical, optical, structural and physicochemical properties. Like graphite, g-C_3N_4 has a two-dimensional planar π conjugation structure, able to enhance the electron transfer processes due to its excellent electronic conductivity.[19] With its medium-sized band gap and its thermal and chemical stability in ambient environment, it has become one of the most promising photocatalytic materials.[19] The interest in its application as a photocatalyst increased after its photocatalytic properties were discovered by Wang et al..[20] However, g-C_3N_4 also has some disadvantages such as a small specific surface area, a small number of active centers, quick recombination of the photo-induced e^-/h^+, low mobility of photoinduced e^-/h^+[21] and an wide band gap (2.7 eV).[22] These shortcomings can be avoided by adding a co-catalyst to g-C_3N_4 to prepare nanocomposites. In recent years, particular interest has appeared in composites of g-C_3N_4 and reduced graphite oxide, rGO, due to the large specific surface area of rGO and its ability to efficiently separate photo-induced charges.[23] The above effect can also be achieved by combining g-C_3N_4 with multi-wall carbon nanotubes.[24] However, these nanocomposites can only solve two of the above disadvantages of g-C_3N_4 as a photocatalyst. The wide band gap of 2.7 eV limits the application of visible light. In order to use g-C_3N_4 as a photocatalyst with visible light, it may be combined with other semiconductor materials with a narrower forbidden zone. Due to its narrow band gap of 1.9 eV, $ZnFe_2O_4$ as a co-catalyst can absorb a wider range of visible light wavelengths. It may also show improved separation of photogenerated electron-hole pairs. Its magnetic properties facilitate the removal of the composites from the reaction mixture, so they can be reused.[25] In the literature available, there are publications presenting studies on triple nanocomposites such as $CoMoS_2$/rGO/C_3N_4 with visible light photocatalytic activity for hydrogen evolution,[26] C_3N_4/rGO/TiO_2[27,28] for decomposition of methyl orange, rhodamine B, and phenol under visible light, and C_3N_4/rGO/WO_3 for degradation of methylene blue.[29] Both the studies mentioned and our experience with $ZnFe_2O_4$ as photocatalyst suggested that $ZnFe_2O_4$/rGO/g-C_3N_4 would be a promising composition to study, as it potentially could overcome g-C_3N_4 shortcomings as photocatalyst as well as take advantage of rGO for the separation of photo-induced charges. The photocatalytic properties of the nanocomposites $ZnFe_2O_4$/rGO/g-C_3N_4 were tested for removal of malachite green as representative pollutant under visible light irradiation, showing better activity than the individual semiconductors. The work presented here on the preparation and the properties of $ZnFe_2O_4$/rGO/g-C_3N_4 can contribute both to the knowledge of inorganic synthesis of such composites and to the improved photocatalytic removal of organic dyes from water.

2. Experimental

2. 1. Materials

Chemicals such as urea (puriss. p.a., Fluka, Switzerland), graphite, $Zn(NO_3)_2 \cdot 6H_2O$, $Fe(NO_3)_3 \cdot 9H_2O$, and $CH_3COONa \cdot H_2O$ (all p.a., Sigma-Aldrich, USA) were used in this study.

2. 2. Synthesis of the Samples

2. 2. 1. Synthesis of Graphitic Carbon Nitride, g-C_3N_4

Thermal polycondensation of urea in a closed crucible at 550 °C for 5 h was applied. The powder was dispersed in water and homogenized by stirring for 1 h, followed by filtering, washing and drying at 50 °C overnight. The successful synthesis was confirmed by XRD and TEM analyses.

2. 2. 2. Synthesis of Reduced Graphene Oxide, rGO

Graphene oxide was prepared by using the modified Hummer's method starting from graphite flakes.[30] In a typical procedure, 0.5 g of graphite was dispersed in 50 mL mixture of conc. H_2SO_4 and conc. H_3PO_4 (volume ratio 9:1) and then ultrasonicated for 1 hour. After that, 6 g of $KMnO_4$ was added and magnetically stirred for 5 h followed by 12 h stirring at 50 °C. The so prepared mixture was cooled to room temperature and transferred in a beaker containing 100 g of ice. After stirring and melting of the ice, 20 mL of 30% H_2O_2 solution was added dropwise in order to remove the unreacted $KMnO_4$. The suspension immediately changed its color from purple to yellow, indicating the formation of graphene oxide. The solid phase was separated by filtration and then dispersed in 100 mL of 5% HCl solution in order to remove all the metal cations and then separated again by centrifugation and washing with water untill a pH = 7. The GO obtained was reduced further to rGO by hydrothermal treatment in a PTFE-lined autoclave at 180 °C for 12 h using hydrazine as a reducing agent.

2. 2. 3. Synthesis of the Composites $ZnFe_2O_4$/rGO/g-C_3N_4

A solvothermal method was used to prepare the composites. The metal salts $Zn(NO_3)_2 \cdot 6H_2O$ and $Fe(NO_3)_3 \cdot 9H_2O$ were dissolved in 50 mL of ethylene glycol, EG, with ratio $n(Zn^{2+}):n(Fe^{3+}) = 1:2$. The rGO was added and dispersed by 30 min magnetic stirring and 2 h of sonication. After g-C_3N_4 was added, the suspension was stirred for 30 min by magnetic stirring, followed by 30 min sonication in an ultrasonic bath. After adding 3 g of $CH_3COONa \cdot 2H_2O$ and stirring for 30 min, the metal ions were precipitated. The mixture was transferred to a 75 mL PTFE autoclave and kept at 180 °C for 24 h. By varying the $ZnFe_2O_4$/g-C_3N_4 mass ratio (0.5, 0.75, 1), three $ZnFe_2O_4$/rGO/g-C_3N_4 composites containing 5 wt% rGO were prepared. They are mentioned further in the text as CN50 ($ZnFe_2O_4$: g-C_3N_4 = 0.5), CN75 ($ZnFe_2O_4$: g-C_3N_4 = 0.75), and CN100 ($ZnFe_2O_4$: g-C_3N_4 = 1).

2. 3. Methods for Characterization of the Samples

X-Ray Diffraction to determine the crystal structure of the materials was performed using a PANalytical Empyrean X-ray diffractometer in the 2θ range of 15–80° using CuKα radiation (λ = 0.15405 nm) for the nanocomposites and in 2θ range of 10–80° for the individual components, steps of 0.01° and 20 seconds exposure time at each step. The average crystallite size was calculated using the well-known Scherrer's equation.[31] The microstructural information of the $ZnFe_2O_4$ was extracted by full profile Rietveld method using the FullProf Suite software.[32] *UV-Vis absorption spectroscopy* was applied using an Evolution 300 UV-Vis spectrometer (Thermo Scientific) for measuring the absorption of the samples in the range of 200-900 nm. *Bandgap energies* were calculated from the UV-Vis absorption spectra in the range from 200 to 400 nm according to Tauc's equation $\alpha h\nu = A(h\nu - E_g)^{n/2}$, where A is a constant independent of $h\nu$, E_g is the semiconductor bandgap and n depends on the type of transition.[33] *Textural characteristics* such as specific surface area, total pore volume, and pore size distribution were determined at –196 °C using a TriStar II 3020 apparatus (Micromeritics). The total pore volume was estimated at a relative pressure P/P_0 0.989. *Transmission electron microscopy* (TEM): a JEOL JEM 2100 microscope was used at 200 kV and up to 100k magnification for characterization of the morphology of the samples. *Particle size distribution analysis* was performed by using ImageJ software.[34]

2. 4. Photocatalytic Tests

The photocatalytic tests were performed using a slurry of 0.5 g catalyst L^{-1} and a 10^{-5} M aqueous solution of Malachite Green oxalate (MG), (Chroma GmbH) as a model pollutant. The equipment and the procedure applied were similar with those used in our previous studies.[14–18,35,36] For illumination 15W white LED (manufactured by V-TAC), 418–700 nm, situated at 10 cm distance above the slurry was used.

3. Results and Discussion

3. 1. Characterization of the Samples

3. 1. 1. Characterization of the Phase Composition by X-ray Diffraction

The phase composition, cell parameters and crystallite size of the samples were determined using the X-ray diffrac-

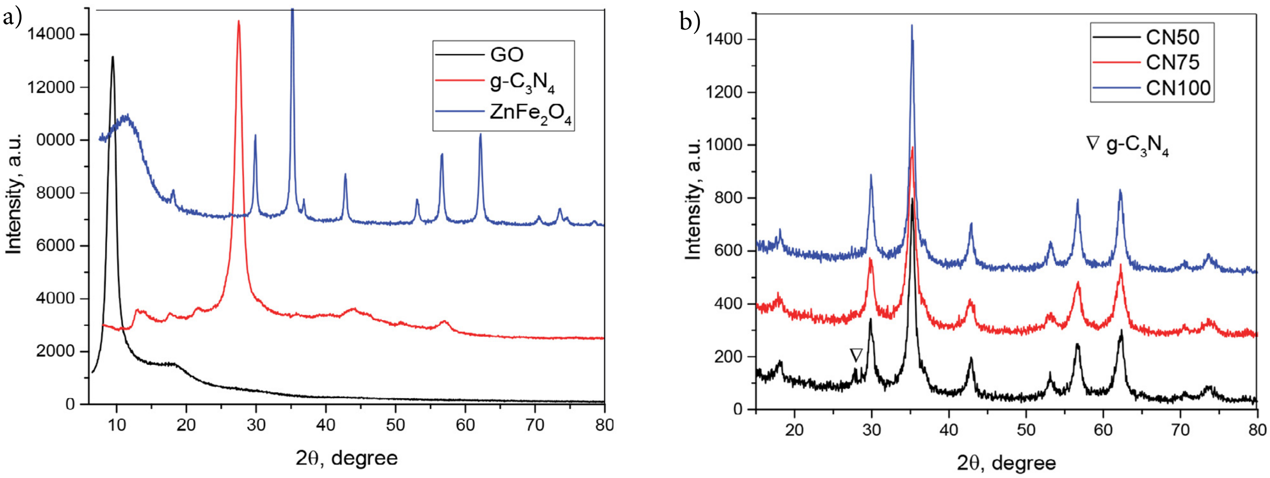

Figure 1. XRD patterns, from bottom to top (a) of the initial samples r-GO, g-C_3N_4, $ZnFe_2O_4$ and (b) of the nanocomposites CN50, CN75, CN100

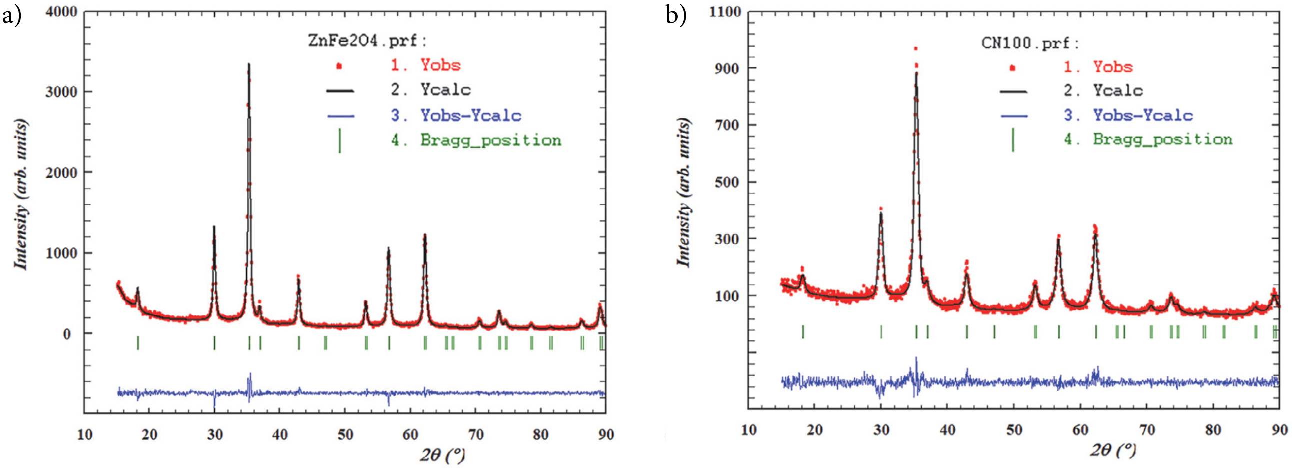

Figure 2. Experimentally observed (dots), Rietveld calculated (continuous line) and difference (continuous bottom line) profiles, obtained after Rietveld analysis of the XRD data (a) $ZnFe_2O_4$ and (b) the composite CN100. Peak positions are shown at the base line as small markers.

tion analysis. The composition of the initial substances r-GO, g-C_3N_4 and $ZnFe_2O_4$ were confirmed (Fig. 1, a). The strong diffraction peak observed at 27° 2theta in the pure g-C_3N_4 can be assigned to the (002) diffraction plane of layered g-C_3N_4 (JCPDS 87-1526) (Fig. 1, a). It corresponds to the characteristic interlayer stacking of aromatic segments.[37] The nanocomposites mainly show the presence of $ZnFe_2O_4$ (Fig. 1, b). The presence of g-C_3N_4 in the composites is detected below 30° 2theta shown by an inversed "Δ" (Fig. 1, b).

Rietveld analysis of the XRD data of $ZnFe_2O_4$ and the composite CN100 was performed (Fig. 2, a, b). The information obtained by the Rietveld refinement was the crystallite size and microstrains as both are related (to extend) to the catalytic properties of the materials.[38,39]

This is also proven by the BET measurements as it can be seen later in the text (Part 3.1.3). On the other side, the microstrains are related to the density of the defects in the crystal structure. The defects, known as active centres in catalysis, are places (especially on the surface) with lower potential energy where the reaction between solid/liquid (or solid/vapor) occurs. Although this is not always true in context of photocatalysis as defects can also act as recombination centres for photogenerated e^-/h^+ pairs leading to lower activity.

The lattice parameters, crystallite size, and the microstrain of the composites and the pure $ZnFe_2O_4$ are shown in Table 1. It can be seen that the increasing content of $ZnFe_2O_4$ in the composites is causing changes in all the parameters mentioned. All the values are getting closer to those of the pure $ZnFe_2O_4$. The microstrain is decreasing in the line 0.0177 (CN50), 0.0147(CN75), 0.0116 (CN100), and 0.0053 for the pure $ZnFe_2O_4$, respectively. The structure of the composites is more defective at lower zinc ferrite content. The latter can be observed in the reduction of the unit cell volume as a result of the microstrains.

3. 1. 2. Characterization of the Sample Morphology by TE

The morphology and the structure of as-synthesized samples observed by TEM are shown in Figure 3. The layered structure of the individual g-C_3N_4 can be seen in Fig. 3, a. The $ZnFe_2O_4$ particles are flower-shaped on the surface of g-C_3N_4 (Fig. 3, b). The electron diffraction of the samples g-C_3N_4 and $ZnFe_2O_4$ is shown in Fig. 3, c, d, respectively. It is used as supplementary analysis to the XRD and approves the successful preparation of $ZnFe_2O_4$ and g-C_3N_4.

With increasing $ZnFe_2O_4$ content in the composites, polydispersed agglomerates are formed. The particle size distribution for CN50 is between 5–10 nm (Fig. 3, e), in accordance with the XRD data.

3. 1. 3. Textural Characterization

Nitrogen adsorption – desorption isotherms measured at –196 °C on powdered samples (Fig. 4, a) showed that the samples are of type IV, which is the typical characteristic of mesoporous materials according to the IUPAC classification.[40] The isotherm of $ZnFe_2O_4$ with H1 loop is typical for well-defined cylindrical pores or agglomerates of approximately uniform spheres (Fig. 4, a). The H3 loop for the g-C_3N_4 and the composites are distinctive for non-rigid aggregates of plate-like particles with slit-shaped pores. The hysteresis loops observed are characteristic of mesoporous solids and their shape exhibits a change in the pore structure. Macropores may be present as well, based on the shape of the hysteresis loops near $P/P_0 = 1$.[41] The average pore size is rather close for the samples g-C_3N_4, CN50 and CN75 (Table 2), while that of $ZnFe_2O_4$ is larger and that of CN100 smaller. The composites show a maximum in the pore size distribution at about 25–50 nm,

Table 1. Lattice parameters, crystallite size and microstrain; CN50 ($ZnFe_2O_4$: g-C_3N_4 = 0.5), CN75 ($ZnFe_2O_4$: g-C_3N_4 = 0.75), and CN100 ($ZnFe_2O_4$: g-C_3N_4 = 1).

Sample	Unit cell, Å	Crystallite size, nm	Microstrain, %	R_{wp}, %	χ^2
CN50	8.4312 ± 0.0007	8 ± 0.2	1.77	9.1	1.74
CN75	8.4321 ± 0.0005	9 ± 0.4	1.47	8.4	1.71
CN100	8.4325 ± 0.0003	11 ± 0.4	1.16	7.9	1.68
$ZnFe_2O_4$	8.4342 ± 0.0002	23 ± 0.3	0.53	7.2	1.53

Table 2. Textural characteristics of the samples studied.

Sample	Specific surface area, S_{BET}, $m^2\,g^{-1}$	Total pore volume, V_{total}, $cm^3\,g^{-1}$	Average pore size, $D_{average}$, nm
g-C_3N_4	88	0.47	22
$ZnFe_2O_4$	34	0.27	32
CN50	72	0.44	25
CN75	77	0.44	23
CN100	67	0.23	14

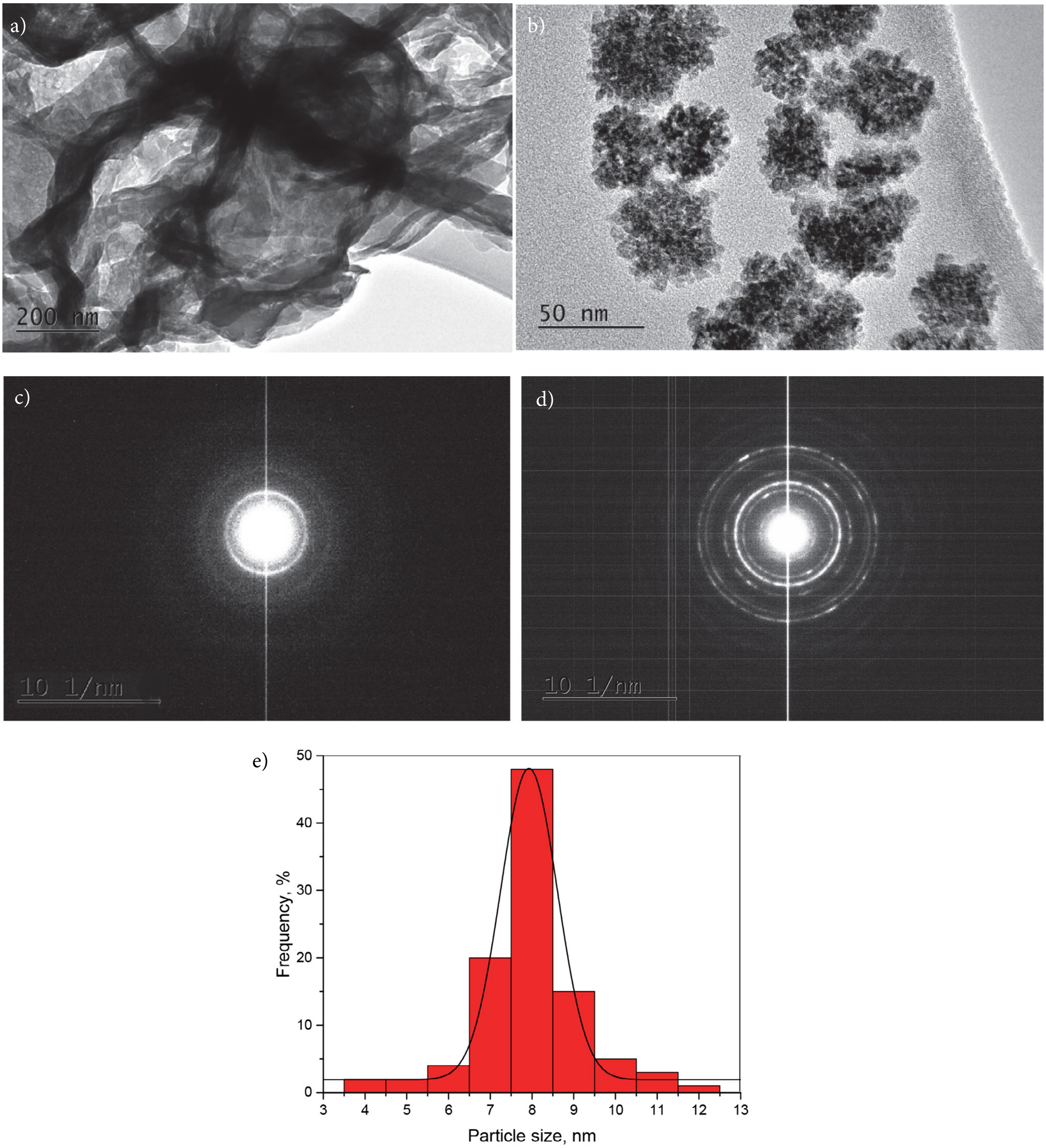

Figure 3. TEM micrographs of (a) g-C_3N_4 and (b) CN50 presented along with the electron diffraction (c) and (d), respectively. The particles size distribution for CN50 is shown in (e).

while CN100 shows a broad polydispersed pore size distribution (Fig. 4, b).

The pure g-C_3N_4 sample has the largest specific surface area, 88 m^2 g^{-1}, while pure $ZnFe_2O_4$ with 34 m^2 g^{-1} has the lowest one among the samples tested (Table 2). In spite of the statement that g-C_3N_4 exhibits low S_{BET},[42] 88 m^2 g^{-1} is a reasonably good value, comparing for example with 9.6 m^2 g^{-1} reported in ref.[42] for g-C_3N_4 obtained by the same hydrothermal method for 48 h/180 °C (12 h/180 °C in present work). Apparently, the duration of the hydrothermal treatment is influencing the agglomeration of the sample. The addition of rGO and $ZnFe_2O_4$ caused a reduction of the specific surface area leading to composites with 77, 72, and 67 m^2 g^{-1} surface area, which could be due to

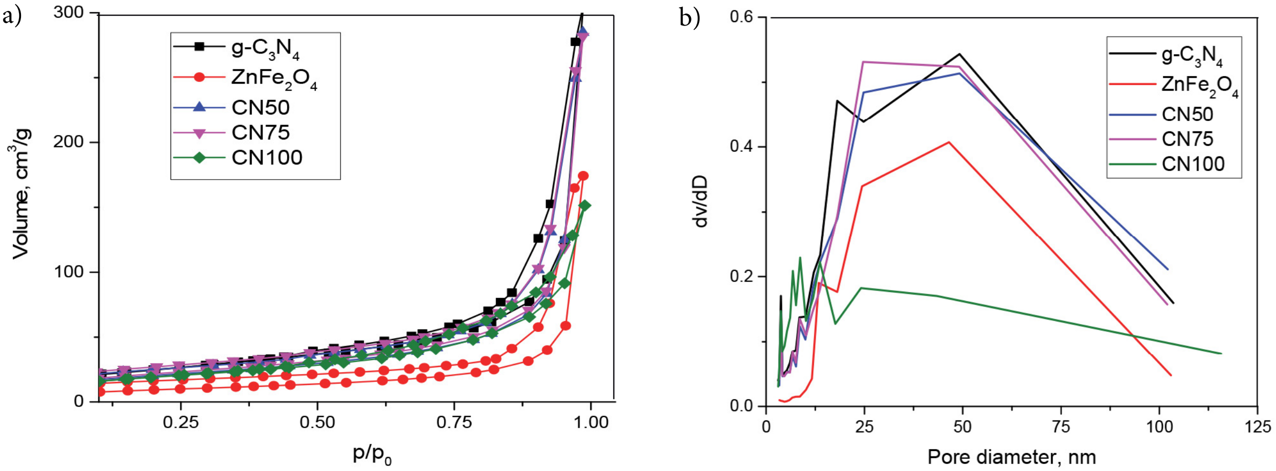

Figure 4. Adsorption-desorption isotherms of the pure g-C_3N_4 and $ZnFe_2O_4$, and the composites CN50, CN75, CN100 (a) and BJH pore diameter distribution, determined from the desorption branch of the isotherm (b); V- pore volume, D – pore diameter.

their deposition on the pores of carbon nitride. Quite likely the presence of g-C_3N_4 inhibits the agglomeration of $ZnFe_2O_4$ particles and makes them uniformly dispersed.

3. 2. Optical and Photocatalytic Properties

3. 2. 1. Optical Properties

The UV/Vis spectra of g-C_3N_4, $ZnFe_2O_4$ and the composites are presented in Fig. 5, a, clearly showing enhanced light absorption of the composites, probably due to interfacial interaction between g-C_3N_4 and $ZnFe_2O_4$.[43] It can be expected that the enhanced light absorption could lead to higher photocatalytic activity by generating more photoinduced charge carriers under visible light. Based on these UV/Vis spectra, the band gap energy was calculated for all the samples (Fig. 5, b). The values for the similar band gaps of the composites with energy of 2.30–2.31 eV (538–536 nm), between the values of g-C_3N_4, 2.7 eV (458

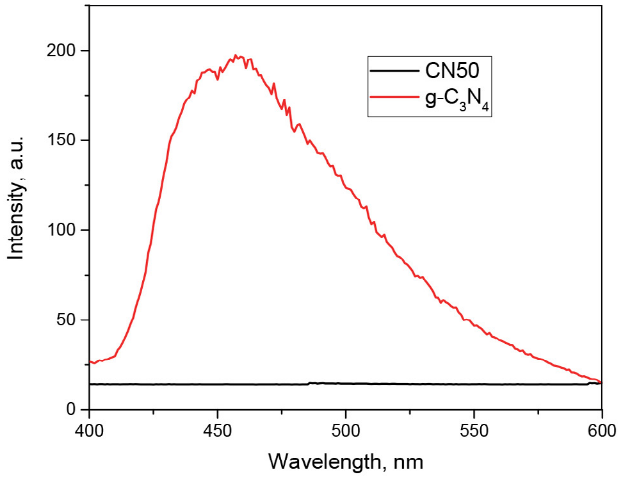

Figure 6. Typical photoluminescence of g-C_3N_4, compared with the absence for CN50.

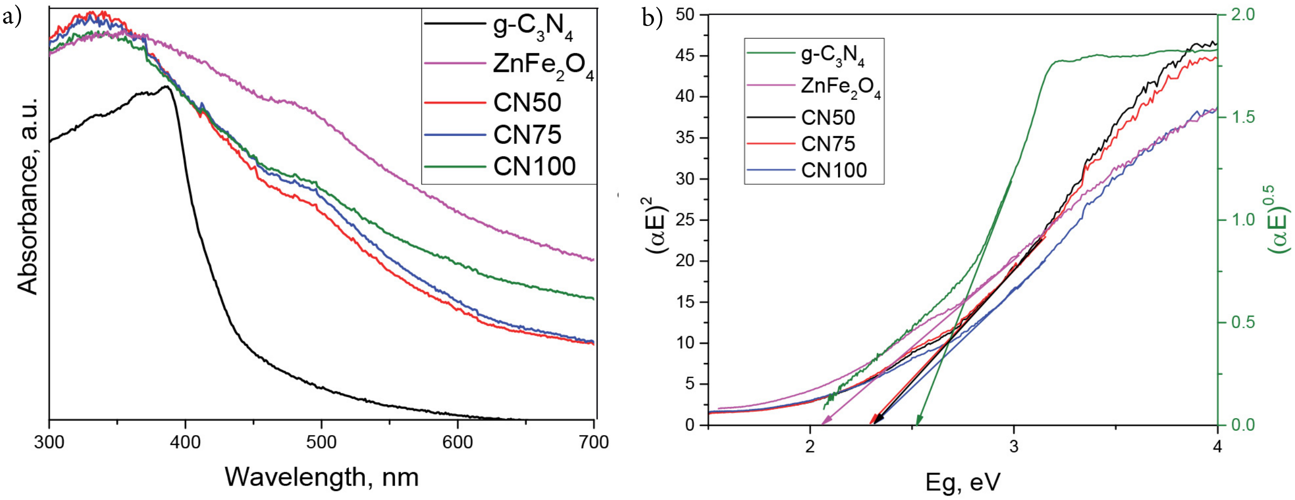

Figure 5. (a) UV/Vis spectra and (b) the energy of the forbidden zone, E_g, for all the samples studied

nm) and $ZnFe_2O_4$, 2.06 eV (600 nm), confirm their prospective for photocatalytic activity higher than that of g-C_3N_4.

Such a prospective is also indicated by the absence of fluorescence in the composites, which provides evidence for efficient inhibition of radiative recombination of photogenerated e^-/h^+ (Fig. 6). The strong fluorescence of the pure g-C_3N_4 related to strong e^-/h^+ recombination (Fig. 6), may explain the low photocatalytic activity of the pristine sample.

3. 2. 2. Degradation of Malachite Green Under Visible Light Irradiation

The photocatalytic performance of the samples for degradation of malachite green under visible light illumination is shown in Fig. 7. In the given range of reaction conditions, adsorption of malachite green on the catalyst surface cannot be neglected (Table 3). However, this was well considered in the subsequent interpretation of collected experimental data. The relevant data for the rate constants are summarized in Table 3.

The rate constant obtained for the photolysis was 0.6 $\times 10^{-3}$ min^{-1}. The pure samples g-C_3N_4 and $ZnFe_2O_4$ showed low values for their rate constants: 2.9 and 4.6 $\times 10^{-3}$ min^{-1}, respectively. The rate constants of the composites were higher, and showed increasing values with increasing $ZnFe_2O_4$/g-C_3N_4 ratio (0.5, 0.75, 1), i.e. 4.0 $\times 10^{-3}$, 5.1 $\times 10^{-3}$ and 7.7 $\times 10^{-3}$ min^{-1}, respectively. Apparently, $ZnFe_2O_4$ and g-C_3N_4 show a synergetic effect, which is best demonstrated for the composite CN100. The highest degradation of malachite green achieved was 63 % for 150 min illumination with visible light. In Table 3, the data for the ratio k/S_{BET} (min^{-1} g m^{-2}) are presented, showing the best activity for $ZnFe_2O_4$, followed closely by the composite CN100.

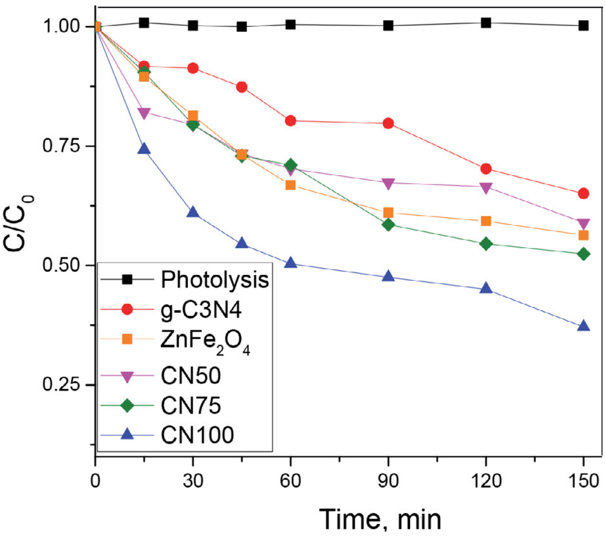

Figure 7. Photocatalytic performance of as-prepared samples for degradation of malachite green under visible-light illumination.

The observed photocatalytic activity may be correlated to the physical properties of the catalysts, such as: *(i)* Surface area: the largest S_{BET} surface area of g-C_3N_4 among the samples tested could provide more active sites to adsorb and convert MG molecules in comparison with the $ZnFe_2O_4$ and the composites. However, this is not observed; g-C_3N_4 may be less active than expected because of its strong e^-/h^+ recombination shown by the fluorescence (Fig. 6). Among the composites, CN100 has less than average S_{BET} but showed the best photocatalytic activity. *(ii)* Large pore volume: it would favor the diffusion of MG molecules within the pores towards the active sites on the surface of the photocatalysts. However, g-C_3N_4 with the largest pore volume shows the lowest activity. *(iii)* Pore size distribution: The composite CN100 has a very broad pore size distribution showing best activity i.e. positively influencing the activity (Fig. 4, b). *(iv)* Bandgap energy: among all samples tested, the composites have the lowest and equal value for E_g but show different activity. Thus the band gap energy alone cannot explain all differences; the activity is determined by a combination of factors. From this it can be concluded that the most active composite CN100 has an optimum combination of band gap value, $ZnFe_2O_4$/g-C_3N_4 ratio and absence of e^-/h^+ recombination. The rGO, being present in equal amounts for all the composites, has the function of solid-state electron mediator,[28, 29] adsorbent, photosensitizer and electron acceptor.[28]

For the discussion of the mechanism of the photocatalytic reaction, the values of the band edges i.e. the potentials of the current band (CB) and the valence band (VB) of the semiconductors $ZnFe_2O_4$ and g-C_3N_4 should be considered. Some of the literature data are summarized

Table 3. Rate constants and extent of malachite green removal based on adsorption on the catalyst surface and degradation.

Sample	Rate constant, $\times 10^{-3}$ min^{-1}	Rate constant to S_{BET}, $\times 10^{-4}$, min^{-1} g m^{-2}	Adsorption, %	Degradation after 150 min, %
g-C_3N_4	2.9	0.395	47	35
$ZnFe_2O_4$	4.6	1.353	63	44
CN50	4.0	0.556	76	41
CN75	5.1	0.66	78	48
CN100	7.7	1.149	86	63

Table 4. Potentials of current band (CB) and valence band (VB) of $ZnFe_2O_4$ and $g\text{-}C_3N_4$.

№	$ZnFe_2O_4$ CB, eV	VB, eV	E_g, eV	$g\text{-}C_3N_4$ CB, eV	VB, eV	E_g, eV	Ref.
1	0.29	2.35	2.06	–1.08	1.54	2.62	Present work
2	0.41	2.38	1.97	–	–	–	45
3	–0.06	1.8	1.76	–1.03	1.64	2.67	42
4	–1.54	0.38	1.92	–1.26	1.34	2.60	40
5	–	–	–	–	1.54	–	43

and presented in Table 4 along with data from our study. It can be seen that in the literature for $g\text{-}C_3N_4$ similar values were reported, i.e. CB -1.03 and VB 1.64 eV[44] as well as –1.26 and 1.34 eV[42]. This is in good agreement with the value for the VB of $g\text{-}C_3N_4$ (1.54 eV) determined by X-ray photoelectron spectroscopy.[45] The literature data for $ZnFe_2O_4$ are less consistent: values observed include –0.06 and 1.8 eV[44] as well as -1.54 eV and 0.38 eV.[42] Taking into account the literature data for the current and valence band it should be mentioned that the CB and VB values for $ZnFe_2O_4$ are lying over those for $g\text{-}C_3N_4$ according to ref.[44] but under values of $g\text{-}C_3N_4$ according to ref.[42] i.e. inconsistency in the data is observed. This can lead to a different way of the interpretation of energy transfer during the photocatalytic process, particularly the migration of electrons and holes between the current band and the valence band of the semiconductors $ZnFe_2O_4$ and $g\text{-}C_3N_4$.

For the samples synthesized $ZnFe_2O_4$ and $g\text{-}C_3N_4$ the band edge positions were evaluated applying the simple equations $E_{VB} = X–E_0+0.5E_g$ and $E_{CB} = E_{VB}–E_g$. The symbols used E_{CB}, E_{VB}, and X are showing the potentials of the conduction band, of the valence band and the electronegativity of the semiconductors $ZnFe_2O_4$ or $g\text{-}C_3N_4$ defined as the geometric average of the absolute electronegativity of the constituent atoms.[46] According the literature data the energy of the free electrons on the hydrogen scale E_0 is about 4.5 eV.[46] For the semiconductors $ZnFe_2O_4$ and $g\text{-}C_3N_4$ the X values were calculated to be 5.82 and 4.73 eV, respectively. Following this, the bottom of current band and the top of valence band were calculated to be –1.08 eV and 1.54 eV for $g\text{-}C_3N_4$, and 0.29 eV and 2.35 eV for $ZnFe_2O_4$, respectively (Table 4). The data for $ZnFe_2O_4$ are in good agreement with data in ref.[47] in spite of the different synthetic method used, influencing the value.

Based on these results, a mechanism for photodegradation of MG over $ZnFe_2O_4$/r-GO/$g\text{-}C_3N_4$ composites can be proposed (Fig. 8). When $ZnFe_2O_4$/r-GO/$g\text{-}C_3N_4$ composites are exposed to visible light, both $ZnFe_2O_4$ and $g\text{-}C_3N_4$ are excited. The photogenerated holes and electrons are in the valence band and conduction band, respectively. $g\text{-}C_3N_4$ can effectively absorb visible light to form photoexcited charge carriers.

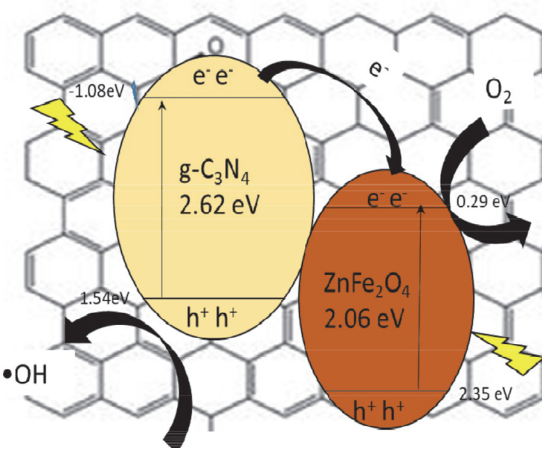

Figure 8. Illustration of the mechanism of the photocatalytic activity of as prepared $ZnFe_2O_4$/GO/$g\text{-}C_3N_4$ samples.

Because the current band of $g\text{-}C_3N_4$ is more negative than that of $ZnFe_2O_4$, the electrons migrate into the current band of $ZnFe_2O_4$; holes in the valence band of $ZnFe_2O_4$ simultaneously migrate to the VB of $g\text{-}C_3N_4$. By this the photogenerated electrons are accumulated on $ZnFe_2O_4$ and holes accumulated on $g\text{-}C_3N_4$. This in turn with water-dissolved oxygen and adsorbed water molecules causes the formation of radicals. These are well known as oxidizing species and as a result MG degradation takes place. The rGO is improving the photocatalytic properties of the composites obtained by efficient separation of photo-induced charges.[23]

4. Conclusions

Nanocomposites of the type $ZnFe_2O_4$/r-GO/$g\text{-}C_3N_4$, based on coupling of two semiconductors, were successfully prepared by applying solvothermal synthesis, where ethylene glycol was used as a solvent. All of the composites, including the stand alone components, were tested and showed activity for photocatalytic degradation of malachite green in aqueous solution under visible light irradiation. The composites show better activity than the pristine $g\text{-}C_3N_4$ and $ZnFe_2O_4$, with the CN100 sample in which $g\text{-}C_3N_4$ and $ZnFe_2O_4$ were present in equal amount showing the highest activity. The improved photocatalytic activity was due to the synergy and the charge transfer between $g\text{-}C_3N_4$ and $ZnFe_2O_4$ as well as the efficient separation of photo-induced charges by rGO. More research has to be done to find the optimum $ZnFe_2O_4$/g-C_3N_4 ratio. The examined composites show potential for degradation of water-dissolved organic pollutants.

Acknowledgements.

M.T. acknowledges the financial support from the program "Young scientists and Postdoctoral candidates" of the Bulgarian Ministry of Education and Science, MCD № 577/2018. The textural measurements were done in Prof. Albin Pintar's Laboratory, National Institute for Chemistry, Slovenia.

5. References

1. J. Longbo, Y. Xingzhong, P. Yang, L. Jie, Z. Guangming, W. Zhibin, W. Hou, *Appl. Catal. B-Environ.* **2017,** *217*, 388–406.
2. E. Sudova, J. Machova, Z. Svobodova, T. Vesely, *Veterinarni Med.* **2007**, *52*, 527–539. **DOI:**10.17221/2027-VETMED
3. N. J. Karrer, G. Ryhiner, E. Heinzle, *Water Res.* **1997**, *31*, 1013–1020. **DOI:**10.1016/S0043-1354(96)00356-9
4. L. Ying-yu, L. Lin, L. Xiao-yan, *J. Clean. Prod.* **2020**, *244*, 118705. **DOI:**10.1016/j.jclepro.2019.118705
5. L. Boutilier, R. Jamieson, R. Gordon, C. Lake, W. Harte, *Water Res.* **2009**, *43*, 4370–4380. **DOI:**10.1016/j.watres.2009.06.039
6. S. Bhattacharjee, S. Datta, C. Bhattacharjee, *Desalination* **2007**, *212*, 92–102. **DOI:**10.1016/j.desal.2006.08.014
7. X. Zi-Peng, S. De-Zhi, *J. Hazard. Mater.* **2009**, *168*, 1264–1268. **DOI:**10.1016/j.jhazmat.2009.03.008
8. S. Zodi, O. Potier, F. Lapicque, J.-P. Leclerc, *Desalination* **2010**, *261*, 186–190. **DOI:**10.1016/j.desal.2010.04.024
9. S. S. Mansouri, I. A. Udugama, A. Mitic, A. Rubin, L. Rudolfsson, K. V. Gernaey, *Comput. Aided Chem. Eng.* **2017**, *40*, 391–396. **DOI:**10.1016/B978-0-444-63965-3.50067-2
10. A. F. S. Foureaux, E. O. Reis, Y. Lebron, V. Moreira, L. V. Santos, M. S. Amaral, L. C. Lange, *Sep. Purif. Technol.* **2019**, *212*, 171–179. **DOI:**10.1016/j.seppur.2018.11.018
11. W. Pronk, A. Ding, E. Morgenroth, N. Derlon, P. Desmond, M. Burkhardt, B. Wu, A. G. Fane, *Water Res.* **2019**, *149*, 553–565. **DOI:**10.1016/j.watres.2018.11.062
12. R. Bochenek, R. Sitarz, D. Antos, *Chem. Eng. Sci.* **2011**, *66*, 6209–6219. **DOI:**10.1016/j.ces.2011.08.046
13. C. Guillard, H. Lachheb, A. Houas, M. Ksibi, E. Elaloui, J. M. Hermann. J. *Photochem. Photobiol. A Chem.* **2003**, *158*, 27–36. **DOI:**10.1016/S1010-6030(03)00016-9
14. R. Kralchevska, M. Milanova, M. Tsvetkov, D. Dimitrov, D. Todorovsky, *J. Mater. Sci.* **2012**, *47*, 4936–4945. **DOI:**10.1007/s10853-012-6368-4
15. R. Kralchevska, M. Milanova, D. Hristov, A. Pintar, D. Todorovsky, *Mater. Res. Bull.* **2012**, *47,* 2165–2177. **DOI:**10.1016/j.materresbull.2012.06.009
16. R. Kralchevska, M. Milanova, P. Kovacheva, J. Kolev, G. Avdeev, D. Todorovsky, *Cent. Eur. J. Chem.* **2011**, *9*, 1027–1038. **DOI:**10.2478/s11532-011-0089-4
17. M. Uzunova-Bujnova, R. Kralchevska, M. Milanova, R. Todorovska, D. Hristov, D. Todorovsky, *Catal. Today* **2010**, *151*, 14–20. **DOI:**10.1016/j.cattod.2010.02.058
18. M. Uzunova-Bujnova, R. Todorovska, M. Milanova, R. Kralchevska, D. Todorovsky, *Appl. Surf. Sci.* **2009**, *256*, 830–837. **DOI:**10.1016/j.apsusc.2009.08.069
19. G. Dong, Y. Zhang, Q. Pan, J. Qiu, *J. Photochem. Photobiol. C Photochem. Reviews* **2014**, *20*, 33–50.
20. X. Wang, K. Maeda, A.Thomas, K. Takanabe, G. Xin, J. M. Carlsson, K. Domen, M. Antonietti, *Nat. Mater.* **2009,** *8*, 76–80. **DOI:**10.1038/nmat2317
21. J. Wen, J. Xie, X. Chen, X. Li, *Appl. Surf. Sci.* **2017**, *391*, 72–123. **DOI:**10.1016/j.apsusc.2016.07.030
22. L. Shi, F. Wang, J. Zhang, J. Sun, *Ceram. Int.* **2016**, *42*, 18116–18123. **DOI:**10.1016/j.ceramint.2016.08.124
23. V. S. Amrutha, K. S. Anantharaju, D. S. Prasanna, *Arabian J. Chem.* **2017**, *10* **DOI:**10.1016/j.arabjc.2017.11.016
24. K. Woan, G. Pyrgiotakis, W. Sigmund, *Adv. Mater.* **2009**, *21*, 2233–2239. **DOI:**10.1002/adma.200802738
25. Q. Ming, S. Qin, W. Guanglei, Zh. Bohan, W. Zhengdong, W. Hongjing, *Mater. Sci. Eng. B* **2017**, *224*, 125–138. **DOI:**10.1016/j.mseb.2017.07.016
26. X. Xuejun, S. Zhichun, L. Liping, W. Zehao, C. Ze, R. Rui, H. Yonghong, W. Duan, *Appl. Surf. Sci.* **2018**, *435*, 1296–1306.
27. M. Huang, J. Yu, Q. Hu, W. Su, M. Fan, B. Li, L. Dong, *Appl. Surf. Sci.* **2016**, *389*, 1084–1093. **DOI:**10.1016/j.apsusc.2016.07.180
28. F. Wu, X. Li, W. Liu, S. Zhang, *Appl. Surf. Sci.* **2017**, *405*, 60–70. **DOI:**10.1016/j.apsusc.2017.01.285
29. G. Zhao, X. Huang, F. Fin, G. Zhang, J. T. S. Irvine, *Catal. Sci. Technol.* **2015**, *6*, 3416–3422. **DOI:**10.1039/C5CY00379B
30. W. S. Hummers, R. E. Offeman, *J. Am. Chem. Soc.* **1958**, *806*, 1339–1339. **DOI:**10.1021/ja01539a017
31. M. Tsvetkov, M. Milanova, L. C. J. Pereira, J. C. Waerenborgh, Z. Cherkezova-Zheleva, J. Zaharieva, I. Mitov, *Chem. Papers,* **2016,** *70,* 1600–1610.
32. J. Rodriguez-Carvajal, *Newsletter*, **2001**, *26*, 12–19.
33. J. Tauc, R. Grigorovici, A. Vancu, *Phys. Status Solidi* **1966**, *15*, 627–637. **DOI:**10.1002/pssb.19660150224
34. C. A. Schneider, W. S. Rasband, K. W. Eliceiri, *Nature methods*, **2012**, *9*, 671–675, PMID 22930834. **DOI:**10.1038/nmeth.2089
35. M. Tzvetkov, M. Milanova, Z. Cherkezova-Zheleva, I. Spassova, E. Valcheva, J. Zaharieva, I. Mitov, *Acta Chim. Slov.* **2017**, *64*, 299–311. **DOI:**10.17344/acsi.2016.3049
36. K. Zaharieva, V. Rives, M. Tsvetkov, Z. Cherkezova-Zheleva, B. Kunev, R. Trujillano, I. Mitov, M. Milanova, *Mater. Chem. Phys.* **2015**, *160*, 271–278. **DOI:**10.1016/j.matchemphys.2015.04.036
37. G. Tzvetkov, M. Tsvetkov, T. Spassov, *Superlattice Microst.* **2018**, *119*, 122–133. **DOI:**10.1016/j.spmi.2018.04.048
38. I. N. Leontyev, A. B. Kuriganova, M. Allix, A. Rakhmatullin, P. E. Timoshenko, O. A. Maslova, A. S. Mikheykin, N. V. Smirnova, *Phys. Status Solidi B* **2018**, 1800240. **DOI:**10.1002/pssb.201800240

39. W. L. Smith, *J. Appl. Crystalography* **1972**, *5*, 127–130. **DOI:**10.1107/S0021889872008921
40. K. S. W. Sing, D. H. Everett, R. A. W. Haul, L. Moscou, R. A. Pierotti, J. Rouquerol, T. Siemieniewska, *Pure Appl. Chem.* **1985**, *57*, 603–604.
41. J. G. Yu, Q. J. Xiang, M. H. Zhou, *Appl. Catal. B-Environ.* **2009**, *90*, 595–602. **DOI:**10.1016/j.apcatb.2009.04.021
42. L. Chen, W. Ma, J. Dai, J. Zhao, C. Li, Y. Yan, *J. Photochem. Photobiol. A* **2016**, *328*, 24–32. **DOI:**10.1016/j.jphotochem.2016.04.026
43. S. Borthakur, L. Saikia, *J. Environ. Chem. Eng.* **2019**, *7*, 103035. **DOI:**10.1016/j.jece.2019.103035
44. S. Patnaik, K. K. Das, A. Mohanty, K. Parida, *Catal. Today*, **2018**, *315*, 52–66. **DOI:**10.1016/j.cattod.2018.04.008
45. W. Hu, J. Yu, X. Jiang, X. Liu, R. Jin, Y. Lu, L. Zhao, Y. Wu, Y. He, *Colloids Surf. A Physicochem. Eng. Asp.* **2017**, *514*, 98–106. **DOI:**10.1016/j.colsurfa.2016.11.058
46. R. Beranek, *Adv. Phys. Chem.* **2011**, *2011*, ID 786759, 20 pages, **DOI:**10.1155/2011/786759
47. L. Jing, Y. Xu, C. Qin, J. Liu, S. Huang, M. He, H. Xu, H. Li, *Mater. Res. Bull.* **2017,** *95*, 607–615. **DOI:**10.1016/j.materresbull.2017.06.003

Povzetek

Nanokompozitni fotokatalizatorji $ZnFe_2O_4$/rGO/g-C_3N_4 z različnimi masnimi razmerji $ZnFe_2O_4$/g-C_3N_4 (0,5; 0,75; 1) so bili pripravljeni z večstopnejsko solvotermalno metodo ter uporabo etilen glikola kot topila. Za karakterizacijo kompozitov so bile uporabljene različne metode, kot so rentgenska difrakcija, UV-Vis spektroskopija in fotoluminiscenčna spektroskopija. Nastanek mezo-/makroporozne strukture s specifično površino med 67 in 77 $m^2\ g^{-1}$ je bil potrjen z adsorpcijo/desorpcijo N_2. Ugotovljeno je bilo, da je v primerjavi z g-C_3N_4 (2,7 eV) širina prepovedanega pasu kompozitov manjša (2,30 eV). V nasprotju s g-C_3N_4, kompoziti niso izkazovali fluorescence, torej ni prišlo do rekombinacije e^-/h^+. Vsi vzorci, vključno s g-C_3N_4 in $ZnFe_2O_4$, so bili testirani za adsorpcijo in fotokatalitično razgradnjo vodnih raztopin zelenega malahita (10^{-5} M) pri obvsevanju z vidno svetlobo ($\lambda > 400$ nm). Rezultati kažejo, da imajo pripravljeni nanokompoziti večjo absorpcijo in fotokatalitično aktivnost kot nemodificirana g-C_3N_4 in $ZnFe_2O_4$ in so zato potencialni kandidati za razgradnjo organskih azobarvil v vodi.